PHOTONICS Research

On-chip terahertz orbital angular momentum demultiplexer

Xiaohan Jiang,[1,†] Wanying Liu,[1,†] Quan Xu,[1,*] Yuanhao Lang,[1] Yikai Fu,[2] Fan Huang,[1] Haitao Dai,[2] Yanfeng Li,[1] Xueqian Zhang,[1] Jianqiang Gu,[1] Jiaguang Han,[1,3,5] and Weili Zhang[4,6]

[1]Center for Terahertz Waves, College of Precision Instrument and Optoelectronics Engineering, and Key Laboratory of Optoelectronics Information and Technology (Ministry of Education), Tianjin University, Tianjin 300072, China
[2]Tianjin Key Laboratory of Low Dimensional Materials Physics and Preparing Technology, School of Science, Tianjin University, Tianjin 300072, China
[3]Guangxi Key Laboratory of Optoelectronic Information Processing, School of Optoelectronic Engineering, Guilin University of Electronic Technology, Guilin 541004, China
[4]School of Electrical and Computer Engineering, Oklahoma State University, Stillwater, Oklahoma 74078, USA
[5]e-mail: jiaghan@tju.edu.cn
[6]e-mail: weili.zhang@okstate.edu
[†]These authors contributed equally to this work.
*Corresponding author: quanxu@tju.edu.cn

Received 24 January 2024; revised 25 February 2024; accepted 3 March 2024; posted 4 March 2024 (Doc. ID 519701); published 1 May 2024

The terahertz regime is widely recognized as a fundamental domain with significant potential to address the demands of next-generation wireless communications. In parallel, mode division multiplexing based on orbital angular momentum (OAM) shows promise in enhancing bandwidth utilization, thereby expanding the overall communication channel capacity. In this study, we present both theoretical and experimental demonstrations of an on-chip terahertz OAM demultiplexer. This device effectively couples and steers seven incident terahertz vortex beams into distinct high-quality focusing surface plasmonic beams, and the focusing directions can be arbitrarily designated. The proposed design strategy integrates space-to-chip mode conversion, OAM recognition, and on-chip routing in a compact space with subwavelength thickness, exhibiting versatility and superior performance.

https://doi.org/10.1364/PRJ.519701

1. INTRODUCTION

Nowadays, there is a growing focus on developing mobile networks that operate at higher frequencies, particularly above 100 GHz, to cater to the ever-increasing demand for information traffic in sixth-generation wireless communication systems [1,2]. The terahertz (THz) wave, specifically within the frequency band of 0.1–10 THz, stands out as an unoccupied and unregulated regime that holds promise for enabling data transmission at very high rates, reaching tens and even hundreds of Gbit/s [3]. This potential has led to the emergence of various techniques such as integrated waveguides [4], wave manipulation [5], direct modulation [6], and multiplexing schemes [7], all aimed at ensuring architectural compatibility for high-level protocols and high-capacity communication. One fundamental technology in the field of THz communication is the efficient modulation of THz waves through wavefront engineering, which allows for facilitating their use in data transmission [8]. Multiplexing is particularly valuable for scenarios that demand ultra-high-speed data transmission and high-capacity applications [9,10]. However, the finite nature of frequency and polarization multiplexing poses limitations on the amount of data that can be transmitted.

To overcome this limitation, vortex beams are being explored as an ideal option to enhance the data-carrying capacity. Vortex beams refer to the light where each photon carries orbital angular momentum (OAM). These beams feature a donut-shaped intensity distribution, a helical phase $\exp(il\varphi)$, and unbounded states $l\hbar$, where the topological charge l can meet the inherent orthogonality to multiplex data streams, φ is the azimuthal angle, and $\hbar$ is the Planck's constant h divided by 2π. The OAM modes can occupy a significantly large mode space, enabling vortex beams with different topological charges to enhance the channel capacity of optical communication [11,12]. Additionally, such beams offer compatibility with conventional techniques such as wavelength-division multiplexing [13] and polarization-division multiplexing [14], making them suitable for deployment in multidimensional THz multiplexing communication systems [15,16].

Benefitting from arrays of subwavelength meta-atoms with meticulous design and appropriate arrangement, metasurfaces

can provide complicated and arbitrary wavefront control capability in a compact and multifunction configuration [17–19]. This capability has attracted extensive attention in various fields such as high-speed communication, information encryption, and quantum entanglement [20–23]. Particularly, there has been increasing interest in the multiplexing and detection of OAM modes using ultrathin and planar metasurfaces [24–29], which has shown great potential in advanced compact systems. However, the availability of mode multiplexers in the THz band is currently limited, hindering the development of highly integrated mode division multiplexing (MDM) systems [30,31]. To address this issue, coupling spatial OAM modes into on-chip systems becomes a crucial step toward ultracompact MDM-based communication [32–34]. Recent advancements in metasurface-based surface plasmon (SP) wave coupling from free-space light have proved various schemes for the detection of physical quantity measurement [35–39] and biochemical sensing [40,41]. Notably, the identification of OAM modes through functional SP devices at dielectric/metal interfaces has garnered significant interest due to their flexibility and compactness [42,43]. However, on-chip OAM demultiplexing in the THz band has not yet been reported, which poses a significant challenge for the development of terminal components required in the MDM-based THz communication.

This study focuses on integrating the scheme of coupling free-space OAM mode into SP modes within an on-chip system operating at THz frequencies. By employing the slit aperture drilled on a metallic film and leveraging its geometric phase, we can identify the OAM of incident circularly polarized vortex beams and guide the coupled SP waves toward predefined directions. We conducted a proof-of-concept experiment, an on-chip OAM mode demultiplexer with seven channels, exhibiting an average isolation level of −11 dB. Near-field THz scanning microscopy (NTSM) was utilized to characterize the performance of the on-chip OAM demultiplexer directly. The experimental results demonstrated excellent directionality. This compact and realizable on-chip device holds potential for applications in THz mode-division-multiplexing communication and OAM-related information processing.

2. RESULTS

A. Holographic Approach to On-Chip OAM Demultiplexer Design

Here we designed a multichannel demultiplexer for selectively coupling space OAM modes to on-chip SP waves by employing the geometric phase [44,45] and the two-dimensional holographic approach [46,47]. The excited SPs can be steered by rotating a set of subwavelength metallic resonators, where the narrow slits drilled on the metallic film are commonly adopted to generate effective dipole sources. In the case of a circularly polarized normal incidence $E_{\mathrm{in}} = (\sqrt{2}/2) \times (1, i\sigma)$ with the helical phase profile of $\exp(il\varphi)$, the orientation of each meta-atom can be determined by the geometric phase control scheme, based on the relationship of $\theta = \Phi/2$ between the geometric phase and the rotation angle of the narrow slits. For simplicity, the basic principle of holography is the reversibility of the light path. As schematically shown in Fig. 1(a), there are n OAM modes working for the left circularly polarized (LCP) incidence corresponding to n imaginary foci located in the x–y plane, where each imaginary focus can be treated as a point SP source at wavelength λ_{SP}, while there are m resonators inside a circular region of radius R arranged in a square lattice with a subwavelength period of Λ along both the x and y directions, composing a hologram to record the scattering information from all imaginary foci. The superposition at the mth dipole source can be written as

$$H_m^{\sigma} = \sum_n \frac{S_n^{\sigma} \exp[-ik_{\mathrm{SP}}|\boldsymbol{r}_{nm}| + i\sigma \arg(\boldsymbol{r}_{nm}) - il_n \arg(\boldsymbol{r}_m)]}{i\sqrt{\lambda_{\mathrm{SP}}|\boldsymbol{r}_{nm}|}}, \tag{1}$$

where S_n^{σ} is the complex coefficient of the nth imaginary point source, and the superscript σ represents the spin direction; $k_{\mathrm{SP}} = 2\pi/\lambda_{\mathrm{SP}}$ is the SP wave number; $\boldsymbol{r}_m$ is the radius vector of the mth dipole source; $\boldsymbol{r}_{nm}$ is the vector from the nth imaginary point source to the mth dipole source and $1/\sqrt{|\boldsymbol{r}_{nm}|}$ is the amplitude decay. The calculation process of the hologram includes the propagation phase profile of $\exp(-ik_{\mathrm{SP}}|\boldsymbol{r}_{nm}|)$, the in-plane phase profile of $\exp[+i\sigma \arg(\boldsymbol{r}_{nm})]$, and the introduced helical phase profile of $\exp[-il_n \arg(\boldsymbol{r}_m)]$. Once the superpositions from all the imaginary foci are obtained, the

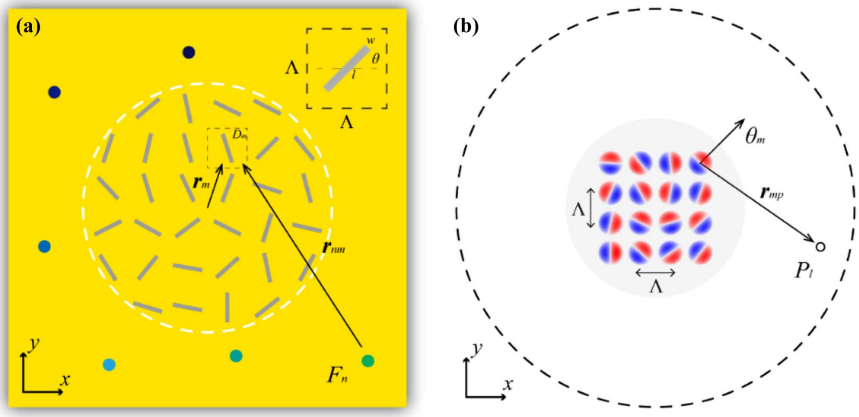

Fig. 1. Schematic views of the holographic design scheme for (a) hologram generation and (b) SP field reconstruction. The parameters are: w, width of the resonator; l, length of the resonator; and θ, rotation angle of the slit resonator.

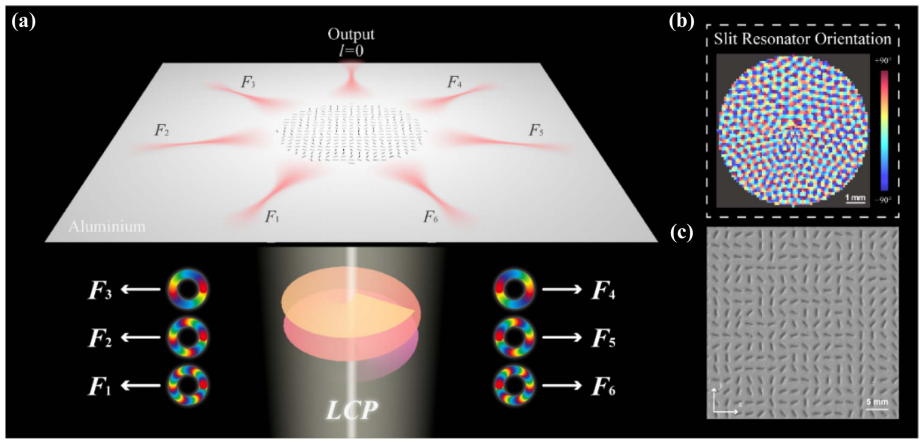

Fig. 2. Seven-channel on-chip OAM modes demultiplexing. (a) Schematic of the on-chip demultiplexer design. (b) Calculated distribution of the resonator orientation angles. (c) Microscopy image of the seven-channel OAM demultiplexer.

orientation angle (the angle between the silt resonator and x-axis) of the mth dipole source can be directly calculated as

$$\theta_m = \arg(H_m^{\sigma})/2. \tag{2}$$

Then the dipole sources emitted from the optimized slit resonators that are drilled on the metallic film are placed at the lattice points with the corresponding rotating angles. As depicted in Fig. 1(b), each dipole source rotated by an angle of θ_m with respect to the x-axis can only be excited by the incident component polarized along its orientation direction and then produce an SP ripple around in the xy-plane. Thus, the superposed SP field at an arbitrary point p from all the resonators under the LCP incidence can be calculated as

$$E_p = \eta \frac{\sqrt{2}}{2} \sum_m \frac{(\cos\theta_m + i\sigma \sin\theta_m) \exp(ik_{\mathrm{SP}}|\boldsymbol{r}_{mp}|) \cos[\theta_m - \arg(\boldsymbol{r}_{mp})] \exp[il_n \arg(\boldsymbol{r}_m)]}{i\sqrt{\lambda_{\mathrm{SP}}|\boldsymbol{r}_{mp}|}}, \tag{3}$$

where $\boldsymbol{r}_{mp}$ is the vector from the center of the mth dipole source to point p, and the complex coefficient η is determined by a realistic resonator. By calculating the superpositions over a region of interest, the space vortex beam to on-chip SP excitation with a specific wavevector for different OAM modes can thus be obtained. Notably, the excited SP waves can be focused by the designed on-chip demultiplexer for high-quality reception of the THz signal.

B. Seven-Channel On-Chip OAM Demultiplexer

Figure 2(a) illustrates a schematic view of a seven-channel vortex-demultiplexing design. Taking advantage of the holographic design principle on a two-dimensional plane, multichannel SP waves coupled from incident vortices will focus to different spots at a radius of 8 mm. The seven focal spots are defined as F_1, F_2, F_3, F_4, F_5, F_6, and F_7 ($l = 0$), where the twirling colorful rings denoting topological charges of 2, 4, and 6 with the positive sign on the left side and the negative sign on the right will be routed to the corresponding SP focusing directions. The SP beam under the LCP incidence ($l = 0$) will be routed to the azimuthal angle of $\pi/2$, and the other output channels are arranged with an angle spacing of $2\pi/7$. The metallic structures of the metasurface containing a total of 5025 slit resonators are periodically arranged with a 100 μm spacing along both the x and y directions inside a circular region with a radius of 4 mm. The center of the circular region is the origin of the in-plane xy coordinate system. For simplicity, each imaginary point source S_n^+ is assigned to 1, and the operating frequency is 0.75 THz. In that way, each resonator (70 μm in length and 10 μm in width) is rotated with the specific orientation angle calculated using Eqs. (1) and (2) under the spin direction of LCP, as shown in Fig. 2(b).

Such slit structures are fabricated with conventional photolithography and metallization processes (see Appendix A for the details). A portion of the fabricated metallic structures are imaged by a microscope and shown in Fig. 2(c).

After the orientation distributions are determined as shown in Fig. 2(b), the numerical results are then calculated using Eq. (3). In the experiment, we obtained the vortex incidences using a series of all-dielectric vortex plates. With the help of the geometric phase in free space, the designed metasurfaces can efficiently convert a Gaussian beam to the vortex beam, and the details can be found in Appendix B. To estimate the performance of these OAM mode convertors, we used NTSM to measure the intensity and phase distributions of the generated vortex beams (see Appendix C for the details), and the measured results are shown in Appendix D. Then the SP fields excited by different vortex beams are mapped by the same THz system. Figure 3(a) exhibits the calculated and measured profiles for OAM incidences with $l = 0$, ± 2, ± 4, and ± 6.

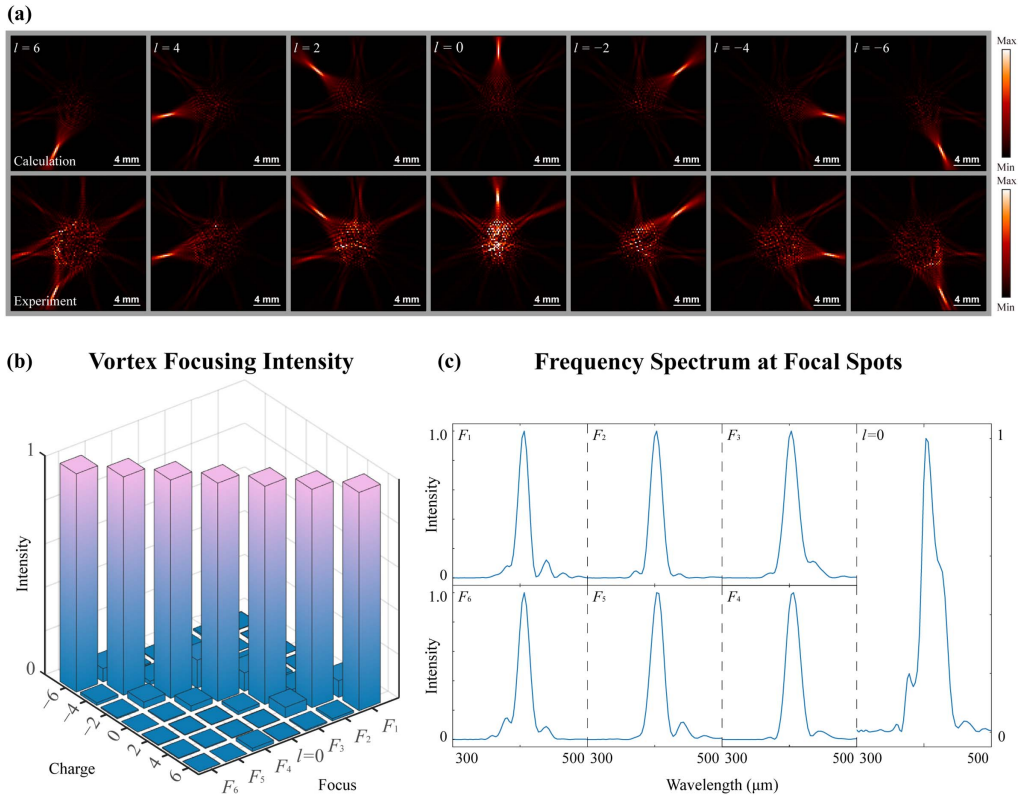

Fig. 3. Results for the seven-channel OAM demultiplexer. (a) Calculated and measured SP intensity distributions. (b) Extracted intensities at focal spots. (c) Frequency spectra at focal spots.

The intensity distribution of E_z in each profile is normalized by the corresponding maximum value of intensity, and the fabrication and measurement errors result in the working frequency being shifted to 0.74 THz. Obviously, seven high-quality focused beams propagating respectively along the predefined directions numerically agree well with our proposed design scheme. For detailed analysis among the transmitted channels, the extracted intensities at focal spots are plotted in Fig. 3(b) to show the crosstalk performance, where the focusing intensities are normalized in the same way. Although there exists slight crosstalk in the analysis, the transmitted energies of the SP beams in the target channels can be detected remarkably, indicating low crosstalk and high isolation in the transmission network. The frequency spectra of the corresponding foci are measured and plotted in Fig. 3(c). The average full width at half maximum is 23 μm, which exhibits good quality in terms of both directionality and frequency response.

C. Performance of On-Chip Demultiplexer under Hybrid OAM Mode Incidences

To estimate the performance of the on-chip demultiplexer under hybrid OAM mode incidences, we applied an interleaved method to design multichannel vortex plates to generate multiple OAM modes simultaneously in Appendix E, and the design scheme is the same as that in our previous work [48]. Figures 4(a) and 4(b) are the calculated and measured SP intensity distributions under the incidence of hybrid OAM modes of $l = 2$ and −2. After comparing the calculated results with the measured ones, we deduce that the unwanted noise and crosstalk in the experiment results are mainly caused by the less perfect design and the misalignment of the incidences. Furthermore, as the total incident energy of the THz transmitting antenna remains constant, the intensity of each component in the hybrid OAM modes is halved compared to the case of single mode OAM incidence. This leads to a decrease in the signal-to-noise ratio of the results shown in Fig. 4(b). However, the SP intensity profiles still reflect the function of the on-chip demultiplexer, and the focusing effect can be observed in two directions. The intensity values at the seven focal spots are extracted and shown in Fig. 4(c), in which the results corresponding to $l = 2$ and −2 channels are remarkably higher than those of the other channels. As for the incidence of three hybrid OAM modes ($l = 2$, −2, and 4), the calculated and measured SP intensity distributions, and extracted intensity values at the focal spots are shown in Figs. 4(d)–4(f), respectively. These results further prove that the proposed SP metasurfaces can effectively demultiplex multiple OAM modes, demonstrating the superior performance of our proposed design scheme in on-demand spatial to on-chip OAM coupling and focusing.

3. DISCUSSION

Although the proposed device is applied for coupling and focusing vortex beams with specific topological charges of 0, ±2, ±4, and ±6, we can design metasurfaces to demultiplex

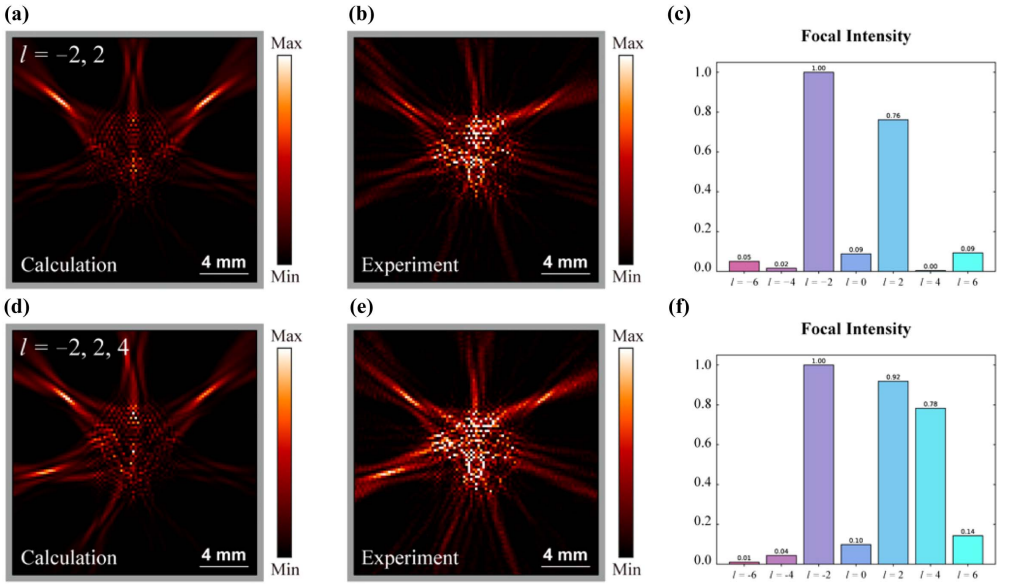

Fig. 4. Performance of the on-chip OAM demultiplexer under the incidence of hybrid OAM modes. (a), (d) Calculated demultiplexed SP intensity distributions under the incidence of two and three hybrid OAM modes, respectively. (b), (e) Corresponding measured results. (c), (f) Extracted intensities at focal spots corresponding to the measured results in (b) and (e).

arbitrary OAM modes based on the holographic method mentioned above. Here, we implement another six-channel demultiplexing with the topological charges of ±1, ±3, and ±5. The schematic of the device and the measured results are shown in Appendix F, indicating the extendibility of our design scheme. Comparing with previous works that have reported on-chip OAM demultiplexing based on a spin-Hall nanograting [42,43], the holographic design has two advantages. One is that propagating directions and focusing spots can be arbitrarily designed; thus SPs can be more flexibly steered on demand. The other is that multidimensional demultiplexing can be further integrated into on-chip devices with the help of the holographic principle, such as wavelength division multiplexing. As shown in Appendix G, we exhibit calculated results of multidimensional demultiplexing for three wavelengths (600 μm, 500 μm, and 400 μm) and three OAM modes ($l = 0$ and ±2). To implement this multidimensional demultiplexing, a proper resonator with the broadband dipole response in SP excitation needs to be adopted for the design. The results demonstrated in this work exhibit the feasibility of space to on-chip OAM demultiplexing. However, the efficiency of the device should be further improved for practical application. A suggested way to decrease the transmission loss of SP waves is connecting a waveguide after focusing and coupling the beam for postprocessing [49,50], which could be considered in our future work.

4. CONCLUSION

We proposed and demonstrated a compact strategy for identifying OAM using a flexible geometric-phase-based control approach on a thin metallic film. By adopting the holographic principle, our on-chip multi-channel OAM demultiplexer operates at THz frequencies and can accurately recognize incident circularly polarized waves with any OAM, including those with a topological charge of zero. The coupled SP waves are efficiently routed in different directions, resulting in low crosstalk and high isolation. These superior performance characteristics make our on-chip SP manipulation technology highly advantageous for signal detection and processing in future communication systems. Our SP demultiplexer not only enables the conversion of OAM into on-chip modes in THz mode-division-multiplexing systems, but also contributes to advancements in the design and fabrication of space-to-on-chip couplers. This progress facilitates flexible steering and high-quality focusing of SPs, thereby promoting the development of on-chip information processing and communication.

APPENDIX A: SAMPLE FABRICATION

The on-chip demultiplexer was fabricated using thermal evaporation, photolithography, and metallization processing. First, a 2-mm-thick double-side-polished high-resistance silicon wafer was deposited with 200-nm-thick aluminum using thermal evaporation. Next, a layer of photoresist (AZ P4000) was spin-coated on the aluminum film and subsequently exposed through UV light to pattern the features for OAM demultiplexing in a mask aligner, and then the patterns were revealed after a development process in AZ400K liquid. In the next step, the aluminum in the structure area was removed by etching, and the remaining photoresist was lifted off by acetone, leaving the aluminum film perforated with the structure on the silicon wafer. In addition to the standard steps above, we spin-coated a 10-μm-thick polyimide layer on the fabricated sample to enhance the confinement of the SPs at the metal surface.

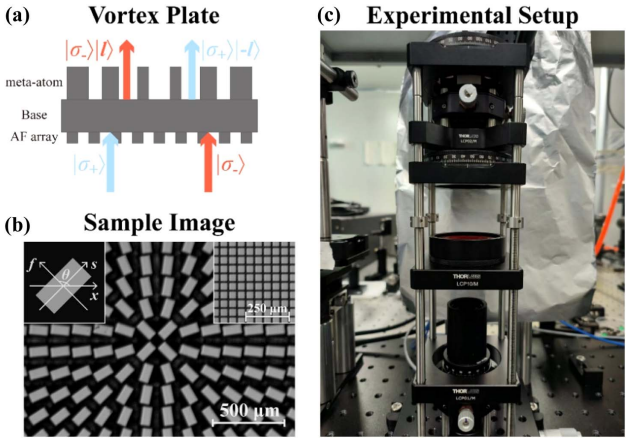

Fig. 5. Generation of incident vortex beams. (a) Schematic of an efficient all-dielectric vortex plate. (b) Microscopy image of a fabricated vortex plate sample ($l = 2$). The inset at the top left corner is the schematic of the square meta-atom, and the image at the top right corner is the anti-reflection layer. (c) Photo of the experimental setup.

APPENDIX B: CONVERTING A GAUSSIAN BEAM TO VORTEX BEAMS

In the last decade, the widespread application of OAM in communications [51], magnetic excitation [52], spinning object detection [53], spiral phase plates [54], computer-generated holograms [55], and spatial light modulators [11] has been exploited to generate vortex beams. However, due to material response and processing technique restrictions, there are limited commercial devices for vortex beam generation in the THz band. In recent years, metasurfaces based on the geometric phase have been widely used in vortex beam generation [56]. Intrinsically, phase manipulation can be encoded into the orientation of the meta-atoms that are carefully optimized with high cross-polarization conversion efficiency under the illumination of LCP and RCP waves. With the help of the geometric phase, we have designed and fabricated a set of metasurfaces for efficient OAM mode conversion in the THz regime, and the generated vortex beams are utilized as incident waves to estimate the performance of our on-chip OAM demultiplexers. Here we use a square silicon pillar as the meta-atom to compose the metasurfaces, which can be regarded as a perfect half-wave plate according to the CST simulation results. The period of this meta-atom is 150 μm, and the lengths of the long and short axes are 130 μm and 66 μm, respectively. As shown in Fig. 5(a), we make a direct connection between the spin states and the OAM using the geometric phase as $|\sigma_{\pm}\rangle \overset{\mathrm{VP}}{\rightarrow} |\sigma_{\mp}\rangle|\pm l\rangle$, where σ is the handedness of incidence and l is the topological charge. There is a relationship of $\theta = \varphi/2$ between the geometric phase and the rotation angle of the silicon pillar. To increase the transmission efficiency of the vortex plates, a polarization-independent anti-reflection layer is adopted [57]. The anti-reflection layer is composed of identical square columns with a length of 40 μm and a height of 54 μm. The period of each square column is 50 μm. With this anti-reflection layer, the multireflection effect at the substrate-air interface can be greatly suppressed to increase transmission efficiency. In the fabrication, we used double-layer reactive ion etching to obtain the dielectric vortex plates. The fabrication process is the same as that in our previous work [58]. The image of a fabricated sample is shown in Fig. 5(b). In this work, 12 different metasurfaces with the required phase profile of $\exp(il\varphi)$ are designed to generate vortex beams with topological charges of $l = -6$ to $l = 6$. The electric fields of the OAM modes are characterized under the circularly polarized incidence by NTSM. In the experiment, a quarter-wave plate is used to convert the linearly polarized beam emitted by a THz photoconductive antenna to a circularly polarized beam. As shown in Fig. 5(c), the THz transmitting antenna, linear polarizer, quarter-wave plate, and vortex plate are integrated into a cage system, thereby simplifying the collimation of the THz path and reducing the impact of replacing the different vortex plates.

APPENDIX C: EXPERIMENTAL SETUP

To experimentally characterize the on-chip OAM-demultiplexing performance, we applied NTSM to directly map the SP fields above the metallic surface. In the experiment, a linearly polarized broadband THz free-space beam was generated from a commercial photoconductive antenna and collimated by a TPX THz lens. Then, a quarter-wave plate was used to convert the linearly polarized beam to a circularly polarized one. After passing through different vortex plates, the beam will carry different topological charges and then be illuminated on the OAM demultiplexers from the substrate side to excite SPs for the demonstration of OAM demultiplexing. It should be noticed that the center of the vortex light must be aligned with that of the sample in the experiment. To avoid this misalignment, we first measured the incident field profiles to determine the centers of incidence. We applied a cage plate mount with the precise removable magnetic plate (Thorlabs, CXY1QF) to make sure of the consistency of the different vortex plates. The sample was finally placed and adjusted under microscopy according to the measured center of light. The SP field was detected by a commercial THz probe that was sensitive to the z-polarized electric field component and placed at ~50 μm above the OAM demultiplexers during the measurement.

APPENDIX D: MEASURED ELECTRIC FIELD DISTRIBUTIONS OF GENERATED VORTEX BEAMS

The measured intensity and phase distributions of the vortex beams are shown in Fig. 6. All the beams exhibit typical donut-shaped intensity distribution, and we can clearly distinguish the topological charges of different OAM modes from the phase distributions shown in Fig. 6. Taking advantage of the wavelength-insensitive property of the geometric phase, the normalized intensity of the generated vortex beams can remain above 85% over a wide frequency range of 0.6–0.9 THz. The efficient generation of the high-purity vortex beams provides the required incidence for the characterization of our on-chip OAM couplers and demultiplexers. In further experiments, the on-chip OAM demultiplexers are placed between a THz

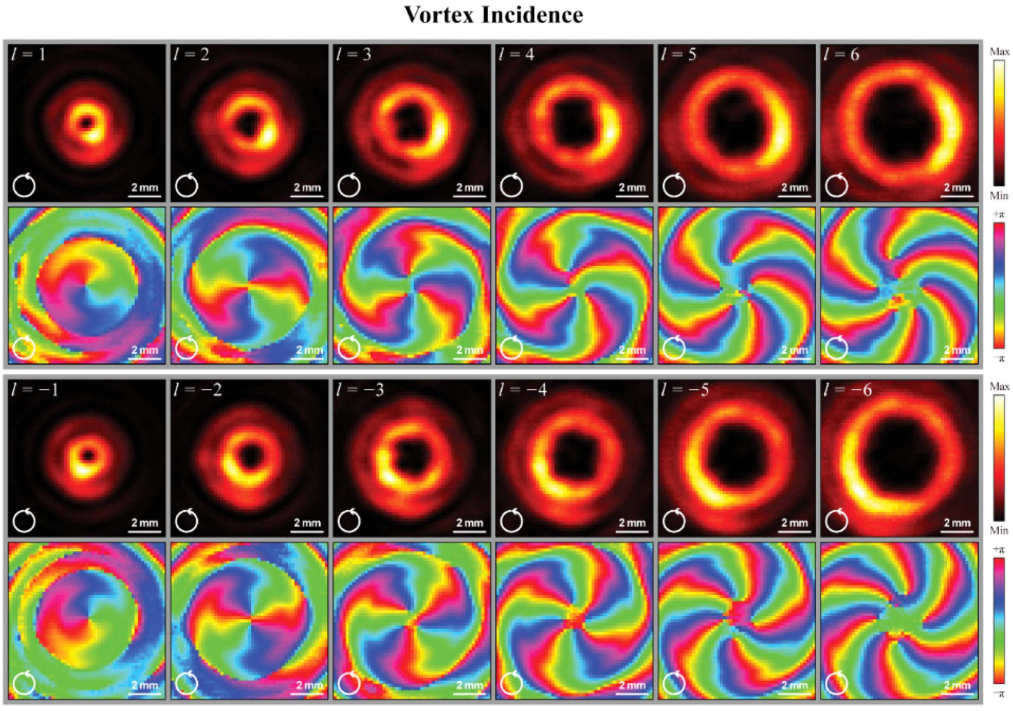

Fig. 6. Measured intensity (first and third rows) and phase (second and fourth rows) distributions of vortex beams with $l = -6$ to $l = 6$ generated by high-efficiency vortex plates.

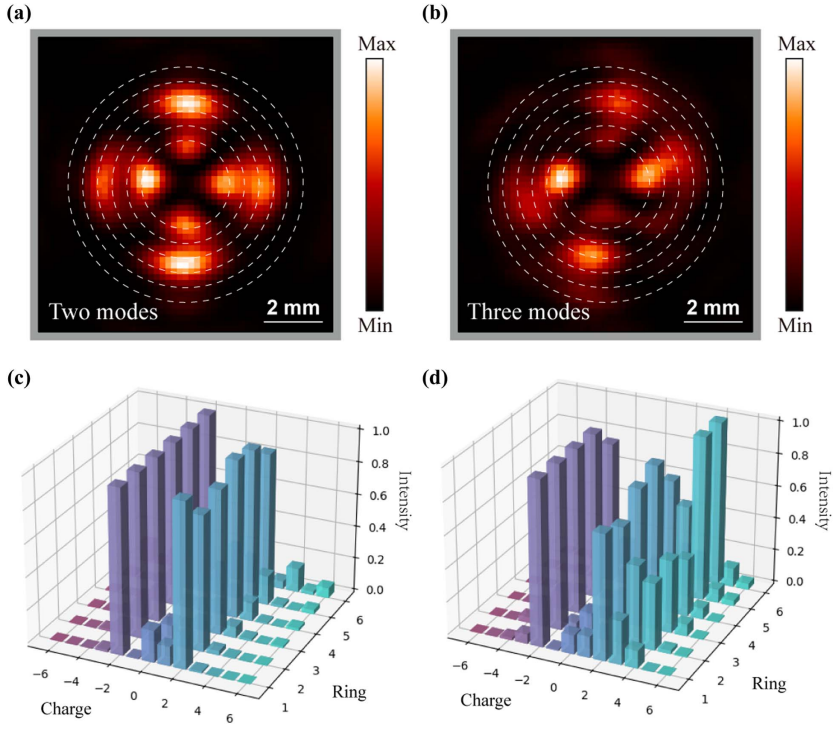

Fig. 7. Measured results of vortex beams with hybrid OAM modes. (a), (b) Measured intensity distributions of vortex beams with two hybrid OAM modes of $l = -2$ and 2 and three OAM modes of $l = -2$, 2, and 4. (c), (d) Normalized intensities of the OAM modes corresponding to (a) and (b) (for l values of −6 to 6) as a function of the radial ring on the beam.

photoconductive probe and the vortex plates. Then we can scan the electric field distributions of the excited surface plasmon waves.

APPENDIX E: METASURFACE-BASED SIMULTANEOUS GENERATION OF MULTIPLE VORTEX BEAMS

To obtain the incident hybrid OAM modes, we use an interleaved method [45,48] to arrange meta-atoms on the basis of the spatial sampling of the phase profiles for the simultaneous generation of multiple vortex beams. Aside from the meta-atom arrangement, these metasurfaces are fabricated using the same material and method as the single-function vortex plates mentioned above. In the experiment, the intensity distributions of the superposed vortex beams with hybrid OAM modes of $l = -2$ and 2 and of $l = -2$, 2, and 4 were measured and are shown in Fig. 7. To estimate the OAM purity of the superposed vortex beams, we selected six radial rings ($r_1 = 1.5$ mm, $r_6 = 4$ mm, and the interval between adjacent rings is

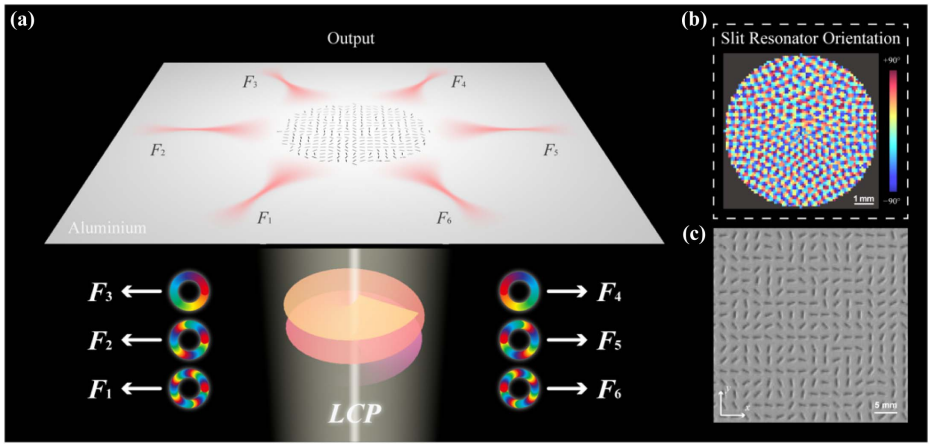

Fig. 8. Six-channel on-chip OAM modes demultiplexing. (a) Schematic of the on-chip demultiplexer design. (b) Calculated distribution of the resonator orientation angles. (c) Microscopy image of the six-channel OAM demultiplexer.

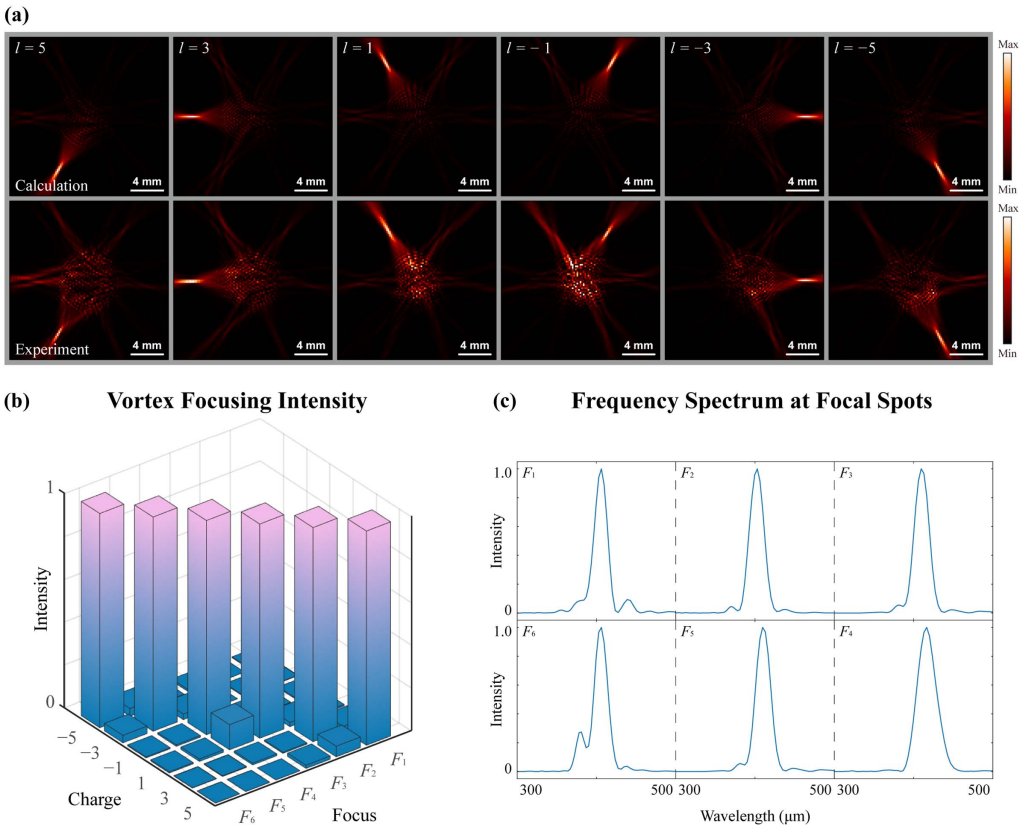

Fig. 9. Results for the six-channel OAM demultiplexer. (a) Calculated and measured SP intensity distribution. (b) Extracted intensities at focal spots. (c) Frequency spectra at focal spots.

0.5 mm) on the beam and calculated the normalized intensity of the OAM modes on each ring by $I_l = [1/2\pi \int_{-\pi}^{\pi} E(\varphi) \exp(-il\varphi) d\varphi]^2$ [59,60]. The results are shown in Figs. 7(c) and 7(d). The normalized intensity on each ring is self-normalized for comparison. For the results of two hybrid OAM modes, it can be observed that the weights of $l = 2$ and −2 channels are remarkably higher than other weights on each ring. As for the results of the three hybrid modes, the weights of $l = 2$ and −2 on the fourth ring are higher than other weights, and the weight of $l = 4$ on rings r_5 and r_6 is relatively higher. This is because the spot diameter of a vortex beam increases with the topological charge. The two types of superposed vortex beams shown in Fig. 7 are used as the incident field to estimate the performance of the on-chip demultiplexers under hybrid OAM mode incidence.

APPENDIX F: SIX-CHANNEL OAM MODES ON-CHIP DEMULTIPLEXING

Taking advantage of the holographic method in Eqs. (1) and (2), metasurfaces can be implemented for demultiplexing arbitrary OAM modes. The metasurface in Fig. 8(a) can couple and focus the vortex beams with $l = \pm 1$, ±3, and ±5. The six focal spots are labeled as F_1 to F_6 in the clockwise direction with an angle spacing of $\pi/3$. Figure 8(b) illustrates the distribution of the resonator orientation angles calculated using the holographic method. This demultiplexer was fabricated in the same way detailed in Appendix A, and an optical image of the sample is shown in Fig. 8(c). Figure 9(a) exhibits the normalized results of calculated and measured profiles at 0.74 THz. The extracted intensities at each focal spot are plotted in Fig. 9(b). The average full width at half maximum is 22 μm, indicating a similarly good directionality and frequency response quality.

APPENDIX G: CALCULATION RESULTS OF NINE-CHANNEL OAM MODES AND WAVELENGTH DEMULTIPLEXING

Based on the holographic design principle, we proposed a nine-channel demultiplexing scheme. The incident beams include three vortex beams at three wavelengths. The calculated results in Fig. 10 display nine focus spots for each channel in different directions, indicating that our strategy holds great promise for multi-dimension demultiplexing.

Funding. National Natural Science Foundation of China (62375203, 61935015, 62027820, 62375200, 62025504, 62075158, 62335011); National Science Foundation (2114103); Yunnan Expert Workstation (202205AF150008).

Disclosures. The authors declare no conflicts of interest.

Data Availability. Data underlying the results presented in this paper are not publicly available at this time but may be obtained from the authors upon reasonable request.

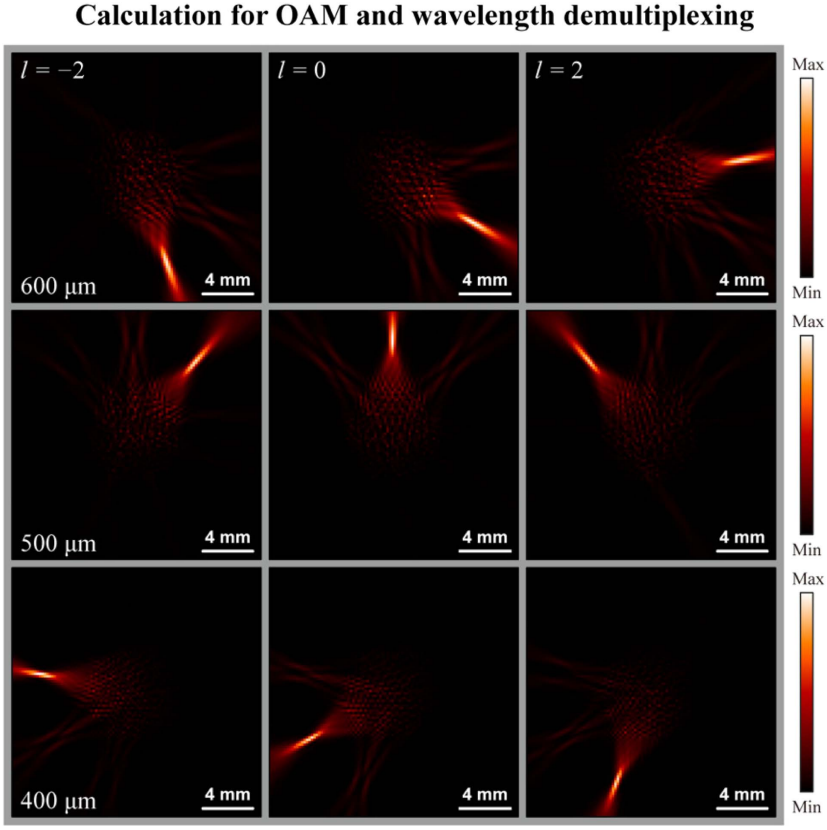

Fig. 10. Nine-channel on-chip OAM and wavelength demultiplexer. The calculated results are implemented under the incidences of topological charges of −2, 0, and 2 and wavelengths of 600 μm, 500 μm, and 400 μm, respectively.

REFERENCES

1. I. F. Akyildiz, J. M. Jornet, and C. Han, "Terahertz band: next frontier for wireless communications," Phys. Commun. **12**, 16–32 (2014).
2. H. Tataria, M. Shafi, A. F. Molisch, *et al.*, "6G wireless systems: vision, requirements, challenges, insights, and opportunities," Proc. IEEE **109**, 1166–1199 (2021).
3. S. Koenig, D. Lopez-Diaz, J. Antes, *et al.*, "Wireless sub-THz communication system with high data rate," Nat. Photonics **7**, 977–981 (2013).
4. A. Kumar, M. Gupta, P. Pitchappa, *et al.*, "Phototunable chip-scale topological photonics: 160 Gbps waveguide and demultiplexer for THz 6G communication," Nat. Commun. **13**, 5404 (2022).
5. Z. Sun, C. Liang, C. Chen, *et al.*, "High-efficiency dynamic terahertz deflector utilizing a mechanically tunable metasurface," Research **6**, 0274 (2023).
6. H. Zeng, H. Liang, Y. Zhang, *et al.*, "High-precision digital terahertz phase manipulation within a multichannel field perturbation coding chip," Nat. Photonics **15**, 751–757 (2021).
7. D. Headland, W. Withayachumnankul, M. Fujita, *et al.*, "Gratingless integrated tunneling multiplexer for terahertz waves," Optica **8**, 621–629 (2021).
8. Y. Zhang, K. Ding, H. Zeng, *et al.*, "Ultrafast modulation of terahertz waves using on-chip dual-layer near-field coupling," Optica **9**, 1268–1275 (2022).
9. J. Ma, N. J. Karl, S. Bretin, *et al.*, "Frequency-division multiplexer and demultiplexer for terahertz wireless links," Nat. Commun. **8**, 729 (2017).
10. Y. Feng, B. Zhang, Y. Liu, *et al.*, "A 200–225-GHz manifold-coupled multiplexer utilizing metal waveguides," IEEE Trans. Microwave Theory Tech. **69**, 5327–5333 (2021).
11. J. Wang, J.-Y. Yang, I. M. Fazal, *et al.*, "Terabit free-space data transmission employing orbital angular momentum multiplexing," Nat. Photonics **6**, 488–496 (2012).
12. Y. Yan, G. Xie, M. P. J. Lavery, *et al.*, "High-capacity millimetre-wave communications with orbital angular momentum multiplexing," Nat. Commun. **5**, 4876 (2014).
13. L.-W. Luo, N. Ophir, C. P. Chen, *et al.*, "WDM-compatible mode-division multiplexing on a silicon chip," Nat. Commun. **5**, 3069 (2014).
14. T. Lei, M. Zhang, Y. Li, *et al.*, "Massive individual orbital angular momentum channels for multiplexing enabled by Dammann gratings," Light Sci. Appl. **4**, e257 (2015).
15. N. Oshima, K. Hashimoto, S. Suzuki, *et al.*, "Terahertz wireless data transmission with frequency and polarization division multiplexing using resonant-tunneling-diode oscillators," IEEE Trans. Terahertz Sci. Technol. **7**, 593–598 (2017).
16. W. Deng, L. Chen, H. Zhang, *et al.*, "On-chip polarization- and frequency-division demultiplexing for multidimensional terahertz communication," Laser Photonics Rev. **16**, 2200136 (2022).
17. J. P. Balthasar Mueller, N. A. Rubin, R. C. Devlin, *et al.*, "Metasurface polarization optics: independent phase control of arbitrary orthogonal states of polarization," Phys. Rev. Lett. **118**, 113901 (2017).
18. A. H. Dorrah, N. A. Rubin, A. Zaidi, *et al.*, "Metasurface optics for on-demand polarization transformations along the optical path," Nat. Photonics **15**, 287–296 (2021).
19. L. Zhang and T. J. Cui, "Space-time-coding digital metasurfaces: principles and applications," Research **2021**, 9802673 (2021).
20. H. Chung, D. Kim, E. Choi, *et al.*, "E-band metasurface-based orbital angular momentum multiplexing and demultiplexing," Laser Photonics Rev. **16**, 2100456 (2022).
21. T. Stav, A. Faerman, E. Maguid, *et al.*, "Quantum entanglement of the spin and orbital angular momentum of photons using metamaterials," Science **361**, 1101–1104 (2018).
22. H. Zhou, B. Sain, Y. Wang, *et al.*, "Polarization-encrypted orbital angular momentum multiplexed metasurface holography," ACS Nano **14**, 5553–5559 (2020).
23. S. Zhang, P. Huo, W. Zhu, *et al.*, "Broadband detection of multiple spin and orbital angular momenta via dielectric metasurface," Laser Photonics Rev. **14**, 2000062 (2020).
24. S. Li, X. Li, L. Zhang, *et al.*, "Efficient optical angular momentum manipulation for compact multiplexing and demultiplexing using a dielectric metasurface," Adv. Opt. Mater. **8**, 1901666 (2020).
25. K. Zhang, Y. Yuan, X. Ding, *et al.*, "Polarization-engineered noninterleaved metasurface for integer and fractional orbital angular momentum multiplexing," Laser Photonics Rev. **15**, 2000351 (2020).
26. Y. Li, X. Li, L. Chen, *et al.*, "Orbital angular momentum multiplexing and demultiplexing by a single metasurface," Adv. Opt. Mater. **5**, 1600502 (2017).
27. R. Zhang, Y. Guo, X. Li, *et al.*, "Angular superoscillatory metalens empowers single-shot measurement of OAM modes with finer intervals," Adv. Opt. Mater. **12**, 2300009 (2023).
28. X. Li, C. Chen, Y. Guo, *et al.*, "Monolithic spiral metalens for ultrahigh-capacity and single-shot sorting of full angular momentum state," Adv. Funct. Mater. **34**, 2311286 (2024).
29. K. Ou, G. Li, T. Li, *et al.*, "High efficiency focusing vortex generation and detection with polarization-insensitive dielectric metasurfaces," Nanoscale **10**, 19154–19161 (2018).
30. H. Zhao, B. Quan, X. Wang, *et al.*, "Demonstration of orbital angular momentum multiplexing and demultiplexing based on a metasurface in the terahertz band," ACS Photonics **5**, 1726–1732 (2018).
31. H. Yang, S. Zheng, H. Zhang, *et al.*, "A THz-OAM wireless communication system based on transmissive metasurface," IEEE Trans. Antennas Propag. **71**, 4194–4203 (2023).
32. P. Genevet, J. Lin, M. A. Kats, *et al.*, "Holographic detection of the orbital angular momentum of light with plasmonic photodiodes," Nat. Commun. **3**, 1278 (2012).
33. Z. Yue, H. Ren, S. Wei, *et al.*, "Angular-momentum nanometrology in an ultrathin plasmonic topological insulator film," Nat. Commun. **9**, 4413 (2018).
34. Y. Lang, Q. Xu, X. Chen, *et al.*, "On-chip plasmonic vortex interferometers," Laser Photonics Rev. **16**, 2200242 (2022).
35. J. S. Q. Liu, R. A. Pala, F. Afshinmanesh, *et al.*, "A submicron plasmonic dichroic splitter," Nat. Commun. **2**, 525 (2011).
36. F. J. Rodríguez-Fortuño, G. Marino, P. Ginzburg, *et al.*, "Near-field interference for the unidirectional excitation of electromagnetic guided modes," Science **340**, 328–330 (2013).
37. S. Liu, T. Jun Cui, A. Noor, *et al.*, "Negative reflection and negative surface wave conversion from obliquely incident electromagnetic waves," Light Sci. Appl. **7**, 18008 (2018).
38. D. Tyagi, T.-Y. Chen, and C.-B. Huang, "Polarization-enabled steering of surface plasmons using crossed reciprocal nanoantennas," Laser Photonics Rev. **14**, 2000076 (2020).
39. J. Han, Y. Xu, H. Zhang, *et al.*, "Tailorable polarization-dependent directional coupling of surface plasmons," Adv. Funct. Mater. **32**, 2111000 (2022).
40. L. Chen, N. Xu, L. Singh, *et al.*, "Defect-induced Fano resonances in corrugated plasmonic metamaterials," Adv. Opt. Mater. **5**, 1600960 (2017).
41. J. Lyu, S. Shen, L. Chen, *et al.*, "Frequency selective fingerprint sensor: the terahertz unity platform for broadband chiral enantiomers multiplexed signals and narrowband molecular AIT enhancement," PhotoniX **4**, 28 (2023).
42. F. Feng, G. Si, C. Min, *et al.*, "On-chip plasmonic spin-Hall nanograting for simultaneously detecting phase and polarization singularities," Light Sci. Appl. **9**, 95 (2020).
43. X. Zhao, X. Feng, F. Liu, *et al.*, "A compound phase-modulated beam splitter to distinguish both spin and orbital angular momentum," ACS Photonics **7**, 212–220 (2020).
44. A. Tomita and R. Y. Chiao, "Observation of Berry's topological phase by use of an optical fiber," Phys. Rev. Lett. **57**, 937–940 (1986).
45. E. Maguid, I. Yulevich, M. Yannai, *et al.*, "Multifunctional interleaved geometric-phase dielectric metasurfaces," Light Sci. Appl. **6**, e17027 (2017).
46. T. V. Teperik, A. Archambault, F. Marquier, *et al.*, "Huygens-Fresnel principle for surface plasmons," Opt. Express **17**, 17483–17490 (2009).
47. X. Jiang, Q. Xu, Y. Lang, *et al.*, "Geometric phase control of surface plasmons by dipole sources," Laser Photonics Rev. **17**, 2200948 (2023).

48. W. Liu, Q. Yang, Q. Xu, *et al.*, "Multichannel terahertz quasi-perfect vortex beams generation enabled by multifunctional metasurfaces," Nanophotonics **11**, 3631–3640 (2022).
49. Y. Zhang, Y. Xu, C. Tian, *et al.*, "Terahertz spoof surface-plasmon-polariton subwavelength waveguide," Photonics Res. **6**, 18–23 (2018).
50. M. Yuan, Q. Wang, Y. Li, *et al.*, "Terahertz spoof surface plasmonic logic gates," iScience **23**, 101685 (2020).
51. A. E. Willner, H. Huang, Y. Yan, *et al.*, "Optical communications using orbital angular momentum beams," Adv. Opt. Photonics **7**, 66–106 (2015).
52. A. A. Sirenko, P. Marsik, C. Bernhard, *et al.*, "Terahertz vortex beam as a spectroscopic probe of magnetic excitations," Phys. Rev. Lett. **122**, 237401 (2019).
53. S. Qiu, Y. Ren, T. Liu, *et al.*, "Spinning object detection based on perfect optical vortex," Opt. Lasers Eng. **124**, 105842 (2020).
54. A. N. Agafonov, Y. Y. Choporova, A. K. Kaveev, *et al.*, "Control of transverse mode spectrum of Novosibirsk free electron laser radiation," Appl. Opt. **54**, 3635–3639 (2015).
55. K. Aoki, A. Okamoto, Y. Wakayama, *et al.*, "Selective multimode excitation using volume holographic mode multiplexer," Opt. Lett. **38**, 769–771 (2013).
56. Y. Zhang, W. Liu, J. Gao, *et al.*, "Generating focused 3D perfect vortex beams by plasmonic metasurfaces," Adv. Opt. Mater. **6**, 1701228 (2018).
57. H. Zhang, X. Zhang, Q. Xu, *et al.*, "High-efficiency dielectric metasurfaces for polarization-dependent terahertz wavefront manipulation," Adv. Opt. Mater. **6**, 1700773 (2018).
58. F. Huang, Q. Xu, W. Liu, *et al.*, "Generating superposed terahertz perfect vortices via a spin-multiplexed all-dielectric metasurface," Photonics Res. **11**, 431–441 (2023).
59. V. V. Kotlyar, A. A. Kovalev, and A. P. Porfirev, "Calculation of fractional orbital angular momentum of superpositions of optical vortices by intensity moments," Opt. Express **27**, 11236–11251 (2019).
60. I. A. Litvin, A. Dudley, and A. Forbes, "Poynting vector and orbital angular momentum density of superpositions of Bessel beams," Opt. Express **19**, 16760–16771 (2011).